



Modeling of lithium plating induced aging of lithium-ion batteries: Transition from linear to nonlinear aging



Xiao-Guang Yang^{a,*}, Yongjun Leng^a, Guangsheng Zhang^a, Shanhai Ge^b,
Chao-Yang Wang^{a,b,**}

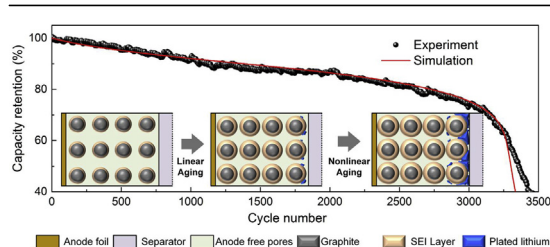
^a Department of Mechanical and Nuclear Engineering and Electrochemical Engine Center (ECEC), The Pennsylvania State University, University Park, PA 16802, USA

^b EC Power, State College, PA 16803, USA

HIGHLIGHTS

- We present a Li-ion battery model capable of predicting Li plating induced aging.
- The model is able to capture the transition from linear to nonlinear aging.
- Nonlinear aging is attributed to exponential increase of Li plating rate.
- Anode porosity drop due to SEI growth is response for onset of Li plating.
- There is positive feedback btw porosity drop and Li plating rate increase.

GRAPHICAL ABSTRACT



ARTICLE INFO

Article history:

Received 4 April 2017
Received in revised form
13 May 2017
Accepted 30 May 2017

Keywords:

Li-ion battery
Lithium plating
Solid electrolyte interphase
Aging
Pore clogging

ABSTRACT

A physics-based Li-ion battery (LIB) aging model accounting for both lithium plating and solid electrolyte interphase (SEI) growth is presented, and is applied to study the aging behavior of a cell undergoing prolonged cycling at moderate operating conditions. Cell aging is found to be linear in the early stage of cycling but highly nonlinear in the end with rapid capacity drop and resistance rise. The linear aging stage is found to be dominated by SEI growth, while the transition from linear to nonlinear aging is attributed to the sharp rise of lithium plating rate. Lithium plating starts to occur in a narrow portion of the anode near the separator after a certain number of cycles. The onset of lithium plating is attributed to the drop of anode porosity associated with SEI growth, which aggravates the local electrolyte potential gradient in the anode. The presence of lithium metal accelerates the porosity reduction, further promoting lithium plating. This positive feedback leads to exponential increase of lithium plating rate in the late stage of cycling, as well as local pore clogging near the anode/separator interface which in turn leads to a sharp resistance rise.

© 2017 Elsevier B.V. All rights reserved.

* Corresponding author.

** Corresponding author. Department of Mechanical and Nuclear Engineering and Electrochemical Engine Center (ECEC), The Pennsylvania State University, University Park, PA 16802, USA.

E-mail addresses: xuy19@psu.edu (X.-G. Yang), cwx31@psu.edu (C.-Y. Wang).

1. Introduction

Aging of lithium ion batteries (LIBs) is a critical issue for applications requiring long life such as electric vehicles (EVs) [1–8].

When expecting a lifespan of 10–15 years for an EV, the durability of LIBs is typically the bottleneck. In general, aging of LIBs involves loss of capacity, rise of impedance, and reduction of power. A fundamental understanding of aging characteristics, such as the evolutions of cell capacity and resistance over the lifetime, is of critical significance for development of reliable life-prediction methods for battery management systems (BMS) [9–11].

Various aging mechanisms have been proposed in the literature, including formation and growth of solid electrolyte interphase (SEI) [3–5], mechanical breakup of electrode materials [12–14], dissolution of transition metals from the cathode [15–17], and deposition of metallic lithium in the anode [18–21]. Among them, SEI growth has been recognized as the dominant aging mechanism in most scenarios, especially for commercially available LIB cells [22–25]. SEI is a layer formed on the surface of electrode materials during the first charge (formation) process. Its role is to protect electrode from further reaction with the electrolyte. Owing to the porous nature of SEI, however, a small amount of electrolyte can still diffuse across the SEI layer and be reduced on the electrode surface after the formation cycle, leading to continuous thickening of the SEI layer and thus loss of active lithium. Dominated by the SEI growth, the capacity decay of LIBs exhibits a square root dependency on time if in storage [26]. If under load, capacity decay is revealed to be linear with respect to the charge throughput [25,26]. Furthermore, both calendar and cycling aging accelerate with the increase of operating temperature, following the Arrhenius law.

In recent years, however, many studies have reported aging behaviors that are in contrast to the above SEI-dominated aging characteristics. One example is the nonlinear capacity drop after prolonged cycling. Schuster et al. [27] cycled a set of commercial 1.95Ah 18650 cells at moderate temperatures and charging rate. Capacity decay and impedance rise were found to be linear with the charge throughput at the beginning, indicating SEI-dominated aging. After prolonged cycling, however, the cell capacity dropped abruptly and cell impedance increased sharply, indicating that some other mechanism took over the aging process. Similar nonlinear aging behaviors have also been reported by other groups [26,28–36]. Based on these research efforts, some major characteristics can be concluded regarding the nonlinear aging phenomenon. First, it occurs for cells of various cathode chemistries, including $\text{LiNi}_{1/3}\text{Mn}_{1/3}\text{Co}_{1/3}\text{O}_2$ (NMC111) [26–29], $\text{LiNi}_{0.6}\text{Mn}_{0.2}\text{Co}_{0.2}\text{O}_2$ (NMC622) [29], LiFePO_4 [30–33], LiCoO_2 [34,35], and LiMn_2O_4 /NMC111 blend [36]. It is therefore reasonable to expect that this nonlinear aging behavior is mostly related to aging mechanisms of the anode. Second, it is revealed that the transition point from linear to nonlinear aging is strongly affected by the current and cut-off voltage of the charging process [27], and also by the composition of the electrolyte [28,34]. Third, through post-mortem analysis of electrodes taken from cells after serious nonlinear aging [27,30–33], thick films were observed near the anode/separator interface, whereas no apparent morphology change was observed for the cathode material. Using energy dispersive X-ray spectroscopy (EDX), Klett et al. [31] showed that the thick films in the anode contain similar composition as the SEI layer. With the help of Osmium tetroxide (OsO_4) staining approach, Zier et al. [37] revealed existence of a large amount of metallic lithium at the anode/separator interface. Broussely et al. [34] also stated that a large deposit of lithium metal was observed after dismantling the deeply cycled cell. Based on the above characteristics, it is believed that the nonlinear aging after prolonged cycling is attributed to lithium plating.

The equilibrium potential of lithium intercalation into graphite is fairly close to, only ~100 mV higher than, the equilibrium potential of lithium deposition reaction. These two reactions therefore compete during cell charging. Under harsh conditions, the anode

potential can become negative with respect to Li/Li^+ [18], leading to deposition of lithium onto the surface of graphite particles instead of intercalation, which is called lithium plating. The plated lithium can react with electrolyte to form a new SEI layer, or can become isolated from the electron-conductive matrix, leading to loss of lithium inventory. Furthermore, the plated lithium metal can be in the form of dendrites, which, in the worst scenarios, may pierce the separator, induce internal short circuit and result in hazardous consequences.

Previously, lithium plating was considered to be a serious issue only under harsh charging conditions like high C-rate and/or low temperatures. Recent work as mentioned above, however, indicates that lithium plating can also occur at mild charge conditions in cells after extended cycling, leading to rapid aging of the cell. One plausible reason for the onset of lithium plating after extended cycling is continuous growth of the SEI layer, which may clog the electrode pores [34] and reduce anode ionic kinetics [27]. The SEI layer can grow considerably after long-term operation. Using focused ion beam (FIB) and scanning electron microscopy (SEM), Yoshida et al. [5] reported that thickness of SEI layer in the tested cells increased from 40 nm at the beginning to as high as 450 nm after storage at 40 °C for 392 days. Lee et al. [38] also revealed via FIB-SEM measurement that the SEI layer of a cell became more than 300 nm thick after 12.5% capacity loss. This significant increase of SEI thickness can greatly reduce the anode porosity, as reported by Frisco et al. [39] most recently. In their work, nano-scale X-ray computed tomography was applied to visualize the pore structure of graphite anode taken from fresh and aged commercial 18650 cells. Dramatic reduction of average pore diameter was observed in the aged cell, with the anode porosity reducing from 0.25 in the fresh cell to 0.12 in the aged cell. This considerable drop of anode porosity can exert strong impacts on cell performance, as discussed by Sikha et al. [40]. However, research efforts on the evolutions of anode porosity and the ensuing impact on cell performance in the aging process are rather scarce in the literature.

Numerical modeling is a useful tool for investigating the aging behavior of LIBs. Numerous physics-based aging models have been proposed in the literature [41–47], most of which focus on capacity fade due to SEI growth. Research on modeling of lithium plating, however, is rather limited [48–52]. Arora et al. [48] proposed the first lithium plating model by incorporating the lithium deposition reaction as a side reaction into the macroscopic LIB model developed by Doyle et al. [53]. The scenario of overcharge was studied and the concentrations of plated lithium at various operating conditions were predicted. Tang et al. [49] extended Arora's model to two dimensional and found that lithium deposition is prone to occur near the edge of anode if the two electrodes are evenly aligned. The importance of using a larger anode than a cathode therefore was stressed. Perkins et al. [50] proposed a method to reduce the complexity of Arora's model in order to develop a control-oriented model suitable for BMS. Most recently, Ge et al. [51] extended Arora's model to the scenario of low temperature charging. The amount of lithium plating is predicted and compared with experiment data measured by nuclear magnetic resonance. To the best of our knowledge, no physics-based aging model has ever been reported in the literature with the ability to predict lithium plating induced aging.

Here, we present a physics-based LIB aging model able to predict aging behaviors associated with lithium plating. It will be demonstrated in the present work that this model is able to capture the above-mentioned transition from linear to nonlinear aging after prolonged cycling. In a companion paper following the present one, the model is applied to study the effects of ambient temperature and electrode thickness on cell aging, as it is known that lithium plating is more prone to occur in cells at low temperatures

and/or with thicker anodes. Detailed descriptions of the model are given in the next section, which has two major features. First, both SEI growth and lithium plating are incorporated in the present model. The competition and interaction between SEI growth and lithium plating can be studied. Second, the drop of anode porosity as a result of SEI growth is considered, and is revealed to be important in affecting the transition from linear to nonlinear aging.

2. Model description

The model presented here is based on our previous electrochemical-thermal (ECT) model [54,55] with modifications to account for lithium plating and SEI growth. The ECT model solves the following governing equations:

Charge conservation in solid electrodes:

$$\nabla \cdot (\sigma_s^{eff} \nabla \phi_s) = j_{tot} \quad (1)$$

Charge conservation in electrolyte:

$$\nabla \cdot (k_e^{eff} \nabla \phi_e) + \nabla \cdot (k_D^{eff} \nabla \ln c_e) = -j_{tot} \quad (2)$$

Species conservation in electrolyte:

$$\frac{\partial(\epsilon c_e)}{\partial t} = \nabla \cdot (D_e^{eff} \nabla c_e) + \frac{1-t_+}{F} j_{tot} \quad (3)$$

Species conservation in active material particles:

$$\frac{\partial c_s}{\partial t} = \frac{1}{r^2} \frac{\partial}{\partial r} \left(D_s r^2 \frac{\partial c_s}{\partial r} \right) \quad (4)$$

Energy conservation of the whole cell (lumped thermal model):

$$m c_p \frac{dT}{dt} = \dot{Q} + hA(T_\infty - T) \quad (5)$$

Detailed descriptions of these governing equations can be found in the literature [54–60] and are therefore not repeated here. Only the modifications made to incorporate lithium plating and SEI growth are detailed below.

In the present model, both SEI growth and lithium plating are considered as side reactions in the anode. Thereby, a total of three electrochemical reactions can occur in the anode, as illustrated in Fig. 1. The desired reaction is lithium intercalation into graphite, following Eq. (6a). The growth of SEI is induced by the formation of new SEI at graphite surface due to the diffusion of electrolyte solvent across the surface film. In this work, the SEI is considered to be made of lithium ethylene dicarbonate ($\text{CH}_2\text{OCO}_2\text{Li}$)₂, generated by the reaction of ethylene carbonate (EC) with Li^+ ions according to Eq. (6b). Furthermore, if the local anode potential becomes negative

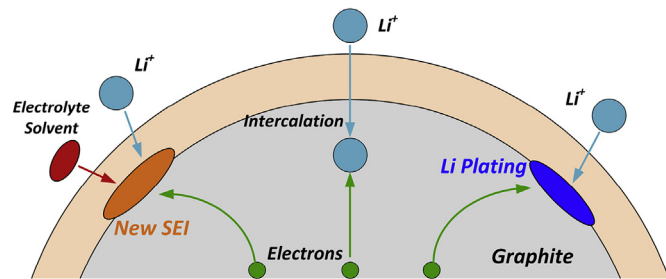
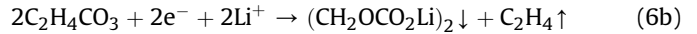


Fig. 1. Schematic illustration of the electrochemical reactions occurring in the anode during cell charging. The main reaction is intercalation of lithium, but lithium can react with solvent molecular to form new solid electrolyte interphase (SEI), or be deposited onto the graphite surface to form metallic lithium.

vs Li/Li^+ , lithium deposition would occur, as described by Eq. (6c). As such, the surface film covering the graphite particles is considered as a mixture of SEI and lithium metal if lithium plating occurs. If not, the surface film contains SEI only.



The total volumetric current density, j_{tot} in Eqs. (1)–(3), are the sum of the current density of all the above three reactions, as:

$$j_{tot} = j_{int} + j_{SEI} + j_{lpl} \quad (7)$$

The transfer current density of lithium intercalation is calculated by the Butler-Volmer equation:

$$j_{int} = a i_{0,int} \left(\exp\left(\frac{\alpha_{a,int} F}{RT} \eta_{int}\right) - \exp\left(-\frac{\alpha_{c,int} F}{RT} \eta_{int}\right) \right) \quad (8)$$

where a is the specific surface area, $i_{0,int}$ is the exchange current density of lithium intercalation, and η_{int} is the surface overpotential defined as:

$$\eta_{int} = \phi_s - \phi_e - \frac{j_{tot} R_{film}}{a} - U_{int} \quad (9)$$

where ϕ_s and ϕ_e are potentials in the solid phase and electrolyte phase; U_{int} is the equilibrium potential for lithium intercalation reaction, and R_{film} is the resistance of the surface film.

According to Safari et al. [44], the rate of SEI formation reaction is affected both by the diffusion rate of EC across the surface film and by the surface kinetics. Following their work, the local current density of SEI formation reaction is calculated by the cathodic Tafel expression below:

$$j_{SEI} = -a F k_{0,SEI} c_{EC}^s \exp\left(-\frac{\alpha_{c,SEI} F}{RT} \left(\phi_s - \phi_e - \frac{j_{tot} R_{film}}{a} - U_{SEI}\right)\right) \quad (10)$$

where $k_{0,SEI}$ is the kinetic rate constant; U_{SEI} is the equilibrium potential of SEI formation reaction, and c_{EC}^s is the concentration of EC on the surface of graphite, which is calculated based on the mass conservation of EC:

$$-D_{EC} \frac{c_{EC}^s - c_{EC}^0}{\delta_{film}} = \frac{j_{SEI}}{F} \quad (11)$$

where D_{EC} is the diffusivity of EC, c_{EC}^0 is the concentration of EC in the bulk electrolyte, and δ_{film} is the thickness of the surface film. The left hand side of Eq. (11) represents the diffusive flux of EC across the film, and the right hand side denotes the consumption rate of EC through reaction (6b).

Lithium plating is assumed to be irreversible in this model. That is, stripping of plated lithium in the subsequent discharge process is neglected. As such, the following cathodic Tafel expression is used to calculate the transfer current density of the lithium deposition reaction:

$$j_{lpl} = -a i_{0,lpl} \exp\left(-\frac{\alpha_{c,lpl} F}{RT} \left(\phi_s - \phi_e - \frac{j_{tot} R_{film}}{a}\right)\right) \quad (12)$$

where $i_{0,lpl}$ is the exchange current density of Li deposition, which is

treated as a fitting parameter in the present model due to the lack of reliable experiment data.

The material balance of SEI and lithium metal can be expressed as:

$$\frac{\partial c_{SEI}}{\partial t} = -\frac{j_{SEI}}{2F} - \frac{j_{pl}}{2F} \beta \quad (13a)$$

$$\frac{\partial c_{Li}}{\partial t} = -\frac{j_{pl}}{F} (1 - \beta) \quad (13b)$$

where c_{SEI} and c_{Li} are the molar concentrations of SEI and lithium metal per unit volume of the electrode. As part of lithium metal in contact with the electrolyte can be oxidized to form new SEI, a parameter of β is introduced which denotes the fraction of plated lithium that becomes SEI. For the sake of simplification, β is assumed to be zero in the present work.

As mentioned above, SEI and lithium metal together constitute the surface film covering graphite particles. In the model, graphite particles are assumed to be spherical, and the surface film is assumed to be uniform in thickness. As such, the amount of SEI and solid lithium can be transformed to an equivalent thickness of the surface film, defined as the ratio of the total volume of SEI and lithium metal to the specific surface area, as:

$$\delta_{film} = \frac{1}{a} \left(\frac{c_{SEI} \cdot M_{SEI}}{\rho_{SEI}} + \frac{c_{Li} \cdot M_{Li}}{\rho_{Li}} \right) \quad (14)$$

where M and ρ are molar weight and density. The left term in the bracket is the specific volume of SEI, and the right term is the specific volume of lithium metal. As stripping of lithium metal is neglected in this model (i.e. all lithium is lost once plated), the plated lithium is considered to be isolated from the main electron-conduction matrix. Hence, resistance of surface film is determined by SEI only, i.e.

$$R_{film} = \omega_{SEI} \frac{\delta_{film}}{\kappa_{SEI}} \quad (15)$$

where ω_{SEI} is the volume fraction of SEI in the film, and κ_{SEI} is its ionic conductivity.

As mentioned above, one feature of the present model is that lowering of anode porosity due to surface film growth is considered, which is implemented through relating the change of anode porosity with the increase of surface film thickness via the following expression:

$$\frac{d\varepsilon}{dt} = -a \frac{d\delta_{film}}{dt} \quad (16)$$

In this work, the above model is applied to study the aging behavior of a LIB cell designed for plug-in EVs cycled at room temperature with moderate charge/discharge current. Cell design information and key model parameters related to SEI growth and Li plating are summarized in Table 1. Parameters on material properties, like solid-phase diffusivity and open-circuit potential of active materials, conductivity and diffusivity of electrolyte, etc., are taken from the material database of AutoLion™ [61,62], a commercial software package for simulation of performance, life and safety of Li-ion batteries.

3. Experimental

A Li-ion pouch cell fabricated by EC Power for plug-in EV applications is tested in this work, which has a nominal capacity of 12.4 Ah and energy density of about 170 Wh/kg. It used graphite as the anode, NMC622 as the cathode, and 1 M of LiPF₆ dissolved in EC/EMC (3:7 by wt.)+2% wt% VC as electrolyte. Detailed design information of the cell is given in Table 1.

The cell was put into cycling test using an Arbin BT-2000 system (Arbin Instruments, TX) at room temperature. In each cycle, the cell was charged using a constant current (CC) step at the rate of 1C to a cut-off voltage of 4.2 V, followed by a constant voltage (CV) step at 4.2 V until the charge current dropped below C/10. Resting for 5 min after the charging process, the cell was discharged at a constant current of 2C to 2.8 V, followed by another 5 min rest before moving to the next cycle. Periodically, the cell was taken off the cycling test and was subject to a series of reference performance tests (RPTs) for evaluation of cell capacity at different discharge rates. The RPTs were performed at an ambient temperature of 25 °C controlled by an environmental chamber (Tenney T10c, Thermal Product Solutions). In each RPT, the cell was charged

Table 1
Cell design information and model parameters.

| Cell Design Information | | | |
|--|-------------------|---------------------------|------------------|
| Parameter | Anode (Graphite) | Separator | Cathode (NMC622) |
| Thickness (μm) | 48.7 | 25 | 40.75 |
| Initial Porosity | 0.32 | 0.4 | 0.33 |
| Loading (mAh/cm ²) | 2.41 | / | 2.0 |
| Electrolyte concentration (mol/L) | / | 1.0 | / |
| Particle radius (μm) | 10 | / | 5 |
| Model parameters related to SEI growth and lithium plating | | | |
| Parameter | Unit | Value | |
| c_{EC}^0 | mol/L | 4.541 [44] | |
| M_{SEI} | kg/mol | 0.162 [44] | |
| ρ_{SEI} | kg/m ³ | 1690 [44] | |
| κ_{SEI} | S/m | 5.0*10 ⁻⁶ [44] | |
| $\alpha_{c,SEI}$ | / | 0.5 [44] | |
| D_{EC} | m ² /s | 2.0*10 ⁻¹⁸ ad | |
| $k_{0,SEI}$ | m/s | 1.0*10 ⁻¹² ad | |
| $\alpha_{c,pl}$ | / | 0.5 | |
| $i_{0,pl}$ | A/m ² | 0.001 ^{ad} | |
| M_{Li} | kg/mol | 6.94*10 ⁻³ | |
| ρ_{Li} | kg/m ³ | 534 | |

^{ad} Adjusted.

using constant current–constant voltage (CCCV) protocol (CC @ 1C to 4.2 V, followed by CV @ 4.2 V to C/20), followed by a 30 min rest, and then discharged at a constant rate of either C/3, 1C, 2C or 3C to a cut-off voltage of 2.8 V.

4. Results & discussion

4.1. Model validation & nonlinear aging behavior

Fig. 2a presents the variation of the 2C discharge capacity during cycling. Both numerical and experimental results are shown and are found to match reasonably well. It is noted from this figure that the 2C discharge capacity decreased linearly with cycle number in the early stage of cycling, from 11.63 Ah at the beginning to 9.13 Ah at the 2700th cycle (~0.93 mAh loss per cycle). Thereafter, cell aging accelerated drastically, with the capacity falling to 6.63 Ah after the 3300th cycle (~4.17 mAh loss per cycle from the 2700th to the 3300th cycle). Though the 2C capacity already dropped below 80% of the initial capacity before the nonlinear decay, which is usually considered as reaching the end of life (EOL) for EV batteries, the highly nonlinear capacity drop at the end has profound impacts on the reuse of LIBs exhausted upon EV operation, e.g. 2nd-life applications in stationary energy storage, as discussed by Schuster et al. [27]. Furthermore, as will be demonstrated in a companion paper,

the transition point from linear to nonlinear aging would shift much earlier in cells with thicker electrodes and/or lower operating temperatures.

Fig. 2b further compares the model and experimental results of the discharge capacity at different C-rates obtained from the RPTs. In experiments, the RPTs were performed periodically by taking the cell off the cycling test as mentioned above. In the model, the rate performance of aged cells are simulated by using cell status parameters stored during cycling as input parameters. These status parameters include lithium stoichiometry, thickness and composition of surface film (e.g. mass of SEI and lithium metal), and local porosity at each mesh grid, which are recorded at the end of each cycle. It can be seen from Fig. 2b that the discharge capacity of each C-rate follows the behavior of linear to nonlinear aging transition. Also, the higher the discharge rate, the earlier the transition point.

To better illustrate the evolution of cell performance of different C-rates over cycling, we plot in Fig. 2c the variation of relative capacity with cycle number. The relative capacity is defined as the ratio of discharge capacity at a given rate to the discharge capacity at C/3 rate. For each C-rate studied, as shown in Fig. 2c, the relative capacity drops slightly in the early state of cycling, indicating that the resistance increase in this process is trivial and cell aging is mainly capacity loss. Thereafter, the relative capacity descends exponentially with cycle number, signifying significant rise of cell

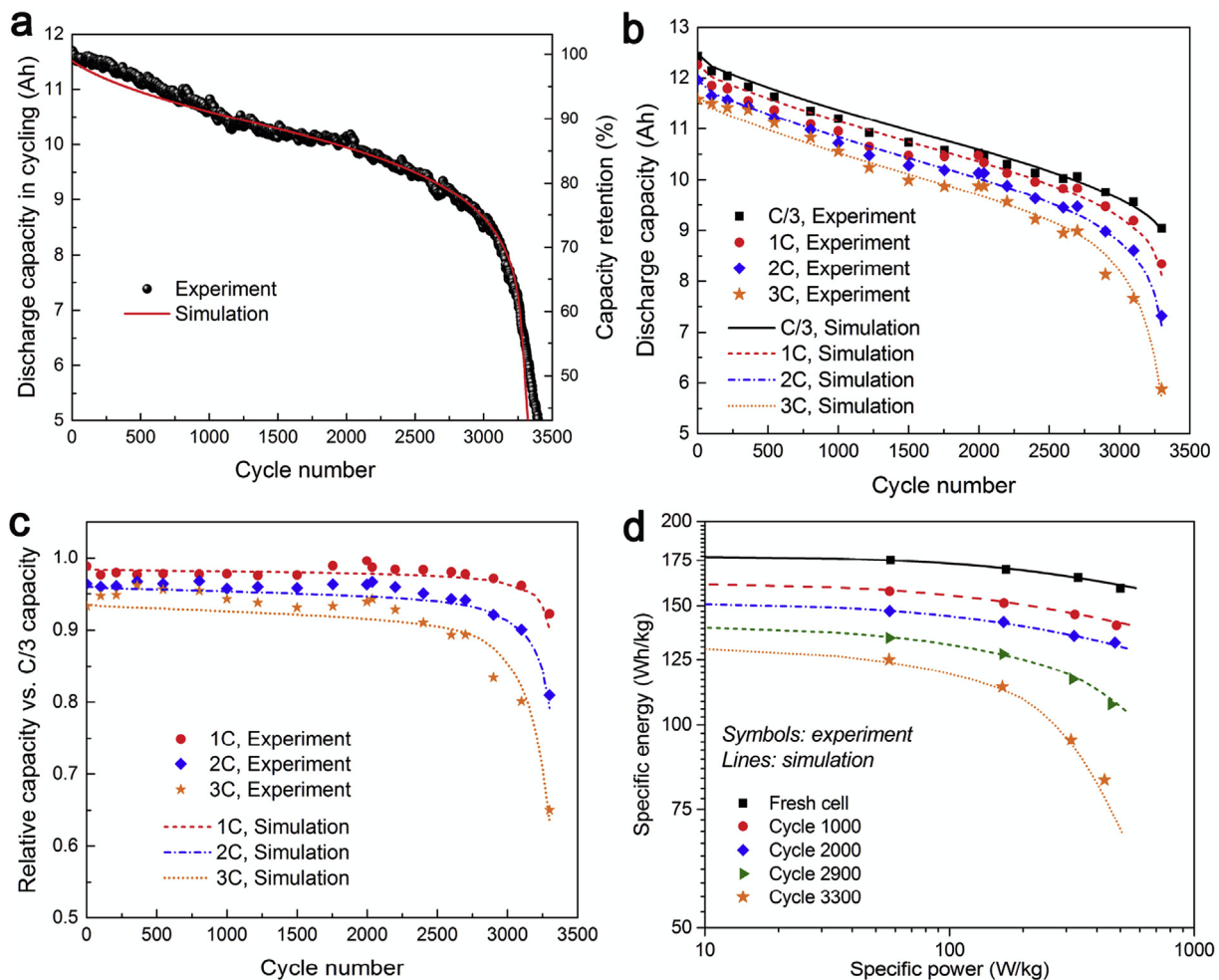


Fig. 2. Comparison of model results with experiment data in terms of (a) variation of discharge capacity with cycle number in the cycling process (2C discharge); (b) variation of cell discharge capacity at C/3, 1C, 2C and 3C rates with cycle number obtained from reference performance tests (RPTs); (c) variation of relative discharge capacity, defined as the ratio of discharge capacity at specified C-rate to the capacity measured at C/3 rate; (d) Ragone plot of the cell after different number of cycles.

resistance. This sharp increase of cell resistance would dramatically deteriorate the power capability of the cell, as can be noted from Fig. 2d where the evolution of Ragone plot upon cell aging is presented. The Ragone plot is an indication of trade-offs between specific energy (SE) and specific power (SP). In this work, the SE and SP of the cell are estimated by the total discharge energy and average discharge power of the cell in the discharge process of the RPTs. As shown in Fig. 2d, the fresh cell is able to deliver 175 Wh/kg SE at the SP of 60 W/kg, and 160 Wh/kg at 500 W/kg. After serious aging (e.g. after 3300 cycles), however, the cell can only deliver ~80 Wh/kg at the SP of ~430 W/kg, though it is still able to deliver 125 Wh/kg at 57 W/kg. If hoping to meet the SP of 500 W/kg, the SE would drop further to <70 Wh/kg.

It can be noted from Fig. 2 that the present model well captures the aging characteristics of the cell over prolonged cycling, from linear capacity fade with slight resistance rise in the early stage, to nonlinear capacity drop with sharp resistance rise in the later stage. Further validation of the model is conducted by comparing the model and experiment results in terms of discharge curves at different C-rates obtained from the RPTs, as shown in Fig. 3. The model results match fairly well with the experiment data for all the cases studied, indicating that the model is able to predict the internal cell characteristics reliably throughout the lifespan of the cell. It can also be noted from this figure that the shape of discharge curves at low C-rates, e.g. C/3 or 1C, is similar across the aging process. The shape of discharge curves at high C-rate, however,

changes dramatically when reaching the nonlinear aging stage. For instance, at 3C discharge as shown in Fig. 3d, the voltage drop at the beginning of discharge is much sharper after the 2900th cycle compared with the discharge curves after the 1000th or 2000th cycle. In the case after the 3300th cycle, cell voltage drops abruptly upon the start of discharge, and then bounces back after reaching a local minimum. This kind of voltage undershoot behavior was reported in the literature for cells discharging in low temperatures [59], and was attributed to the poor electrolyte performance at freezing temperatures. For cells discharging at room temperature, to the best of our knowledge, this anomalous behavior of voltage undershoot has never been reported. Reasons for this behavior will be discussed in the following section.

4.2. Resistance rise due to local pore clogging near anode/separator interface

We can learn from Figs. 2 and 3 that cell resistance increases exponentially after prolonged cycling and leads to dramatic change in the shape of discharge curve at high C-rate. To explore the underlying reasons for these phenomena, the voltage loss during 3C discharge are analyzed in detail for the fresh and aged cells. Following the work of Ji et al. [59], the overall voltage loss is broken down into those due to (1) electrical resistance in electrode; (2) charge transfer resistance at active material/electrolyte interface; (3) ionic conduction resistance and concentration polarization in

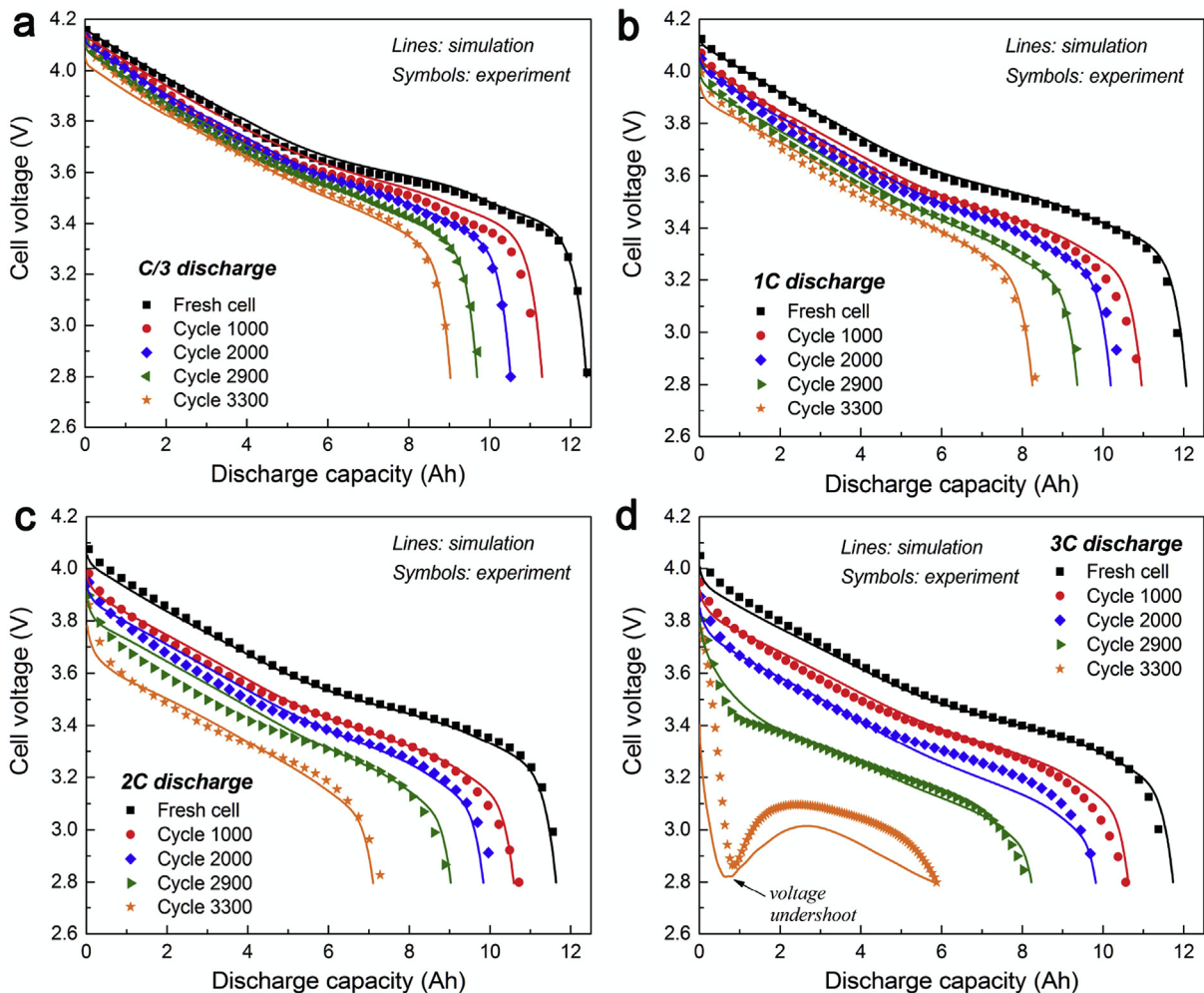


Fig. 3. Comparison of model results with experiment data in terms of discharge curves at (a) C/3 (b) 1C (c) 2C and (d) 3C measured in the reference performance tests of the cell after different number of cycles.

electrolyte (hereafter referred to as electrolyte resistance); (4) concentration polarization inside solid active materials, and (5) electrical resistance due to imperfect contact between individual components. Detailed definitions of and methods for calculation of these individual voltage losses can be found in Ref. [59]. Fig. 4a–c presents the evolution of the individual voltage losses during 3C discharge of the fresh cell and of the cell after 2000 and 3300 cycles. The cell after 2000 cycles is representative for linear aging stage,

and that after 3300 cycles denotes the cell after serious nonlinear decay. Voltage losses due to (1) & (5) are not shown in these figures as the electrical resistance is negligible in the electrodes, and the electrical contact resistance are assumed to be constant over the entire cell life.

It can be seen from Fig. 4a–c that the increase of cell resistance during aging mainly includes the rise of anode electrolyte resistance and of anode charge transfer resistance. The latter is caused

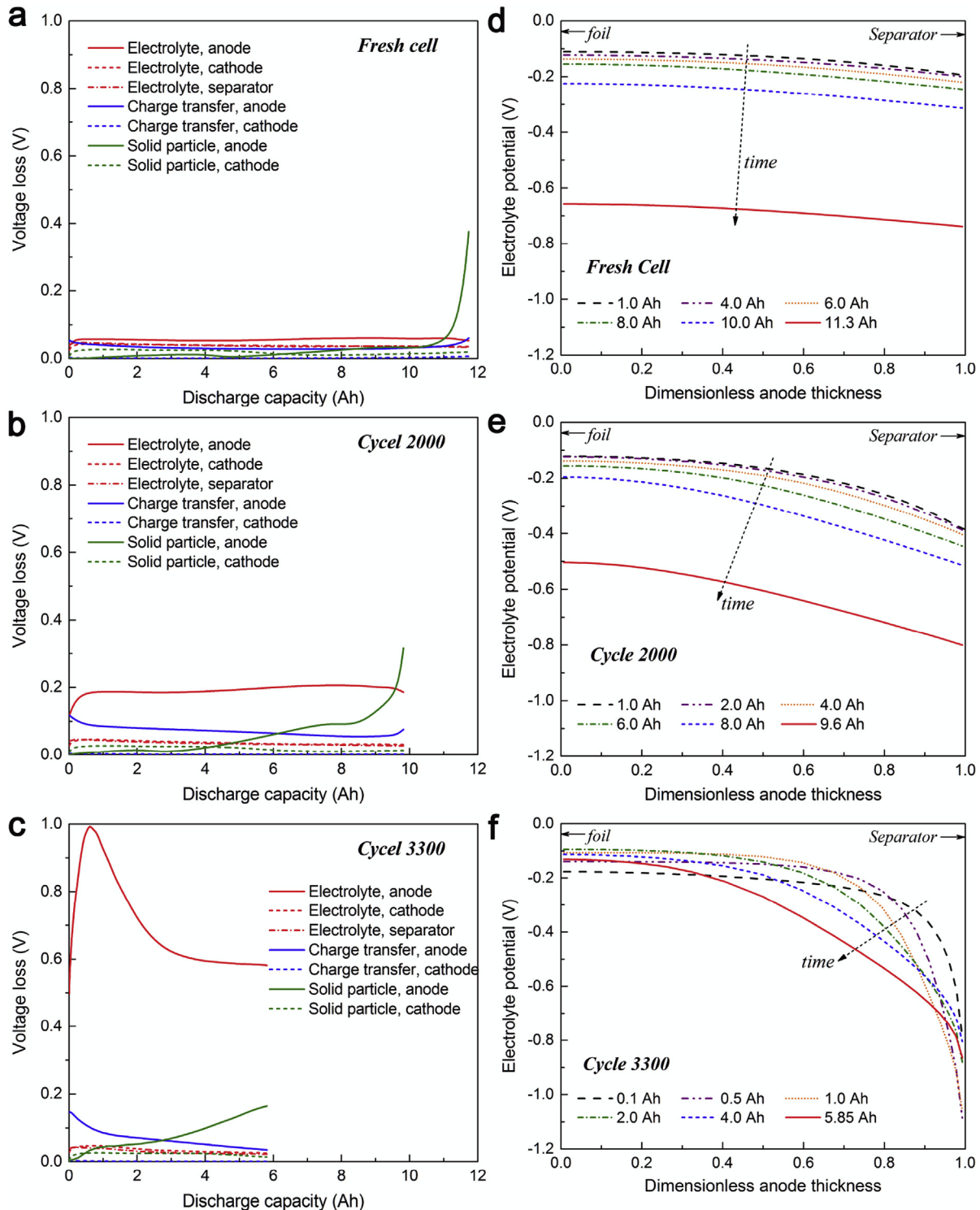


Fig. 4. (a–c) Analysis of voltage losses due to different mechanisms and (d–f) distributions of electrolyte potential across the anode thickness in the 3C discharge process of (a&d) fresh cell, (b&e) cell after 2000 cycles and (c&f) cell after 3300 cycles.

by SEI layer growth, and is smaller than the former. Comparing the anode electrolyte resistance in the three figures we can conclude that the anode electrolyte resistance increases moderately in the linear aging stage but sharply in the nonlinear aging stage. The rapid rise of anode electrolyte resistance after extended cycling is expected to dictate the rapid drop of the 2C capacity in the late stage of cycling (Fig. 2a). Furthermore, as shown in Fig. 4c for the cell after 3300 cycles, the anode electrolyte resistance ascends steeply upon the start of discharge to a local peak, and begins to decrease afterwards. This overshoot behavior of anode electrolyte resistance is expected to be responsible for the voltage undershoot observed in Fig. 3d.

The anode electrolyte resistance is defined as the difference between the volume-averaged electrolyte potential of the anode and the electrolyte potential at the anode/separator interface. Fig. 4d and 4f present the distributions of electrolyte potential across the anode in the above three cases. As ionic current moves from anode to cathode in discharge, the electrolyte potential in the anode decreases from the foil to the separator. The total drop of electrolyte potential in the anode is fairly small in the fresh cell as shown in Fig. 4d, and increases moderately in the linear aging process as can be drawn from Fig. 4e. In the case after severe nonlinear aging (Fig. 4f), a huge drop of electrolyte potential appears near the anode/separator interface, especially at the beginning of discharge.

The rise of anode electrolyte resistance during aging is mainly induced by the decrease of anode porosity over cycling, as shown in Fig. 5a where the distribution of local porosity in the anode is plotted for cells after different number of cycles. It can be noted that the anode porosity decreases in the cycling process. In the early stage (e.g. <2000 cycles), the local porosity is relatively uniform across the anode. Thereafter, however, the local porosity drops sharply in the region close to the separator. After 3300 cycles, the porosity near the anode/separator interface becomes even lower than 0.05, indicating clogging of pores.

The reduction of porosity is attributed to the growth of surface film as described by Eq. (16). As mentioned above, both the formation of new SEI and the deposition of lithium metal can contribute to surface film growth. Fig. 5b and c presents the percentage of pore volume occupied by the SEI and by the deposited lithium metal respectively in the cycling process. The growth of SEI layer, as shown in Fig. 5b, is moderate and relatively uniform across the anode in the entire cycling process. Lithium metal, however, appears only after ~2000 cycles and only in a very narrow region near the separator. Nevertheless, the accumulation rate of lithium metal increases significantly in the late stage of cycling, which is responsible for the rapid drop of local porosity near the separator shown in Fig. 5a. The relative volume fractions of free pores, SEI layer and lithium metal along the anode thickness are plotted in Fig. 5d for the cell after 3300 cycles. It can be noted that ~40–50% of

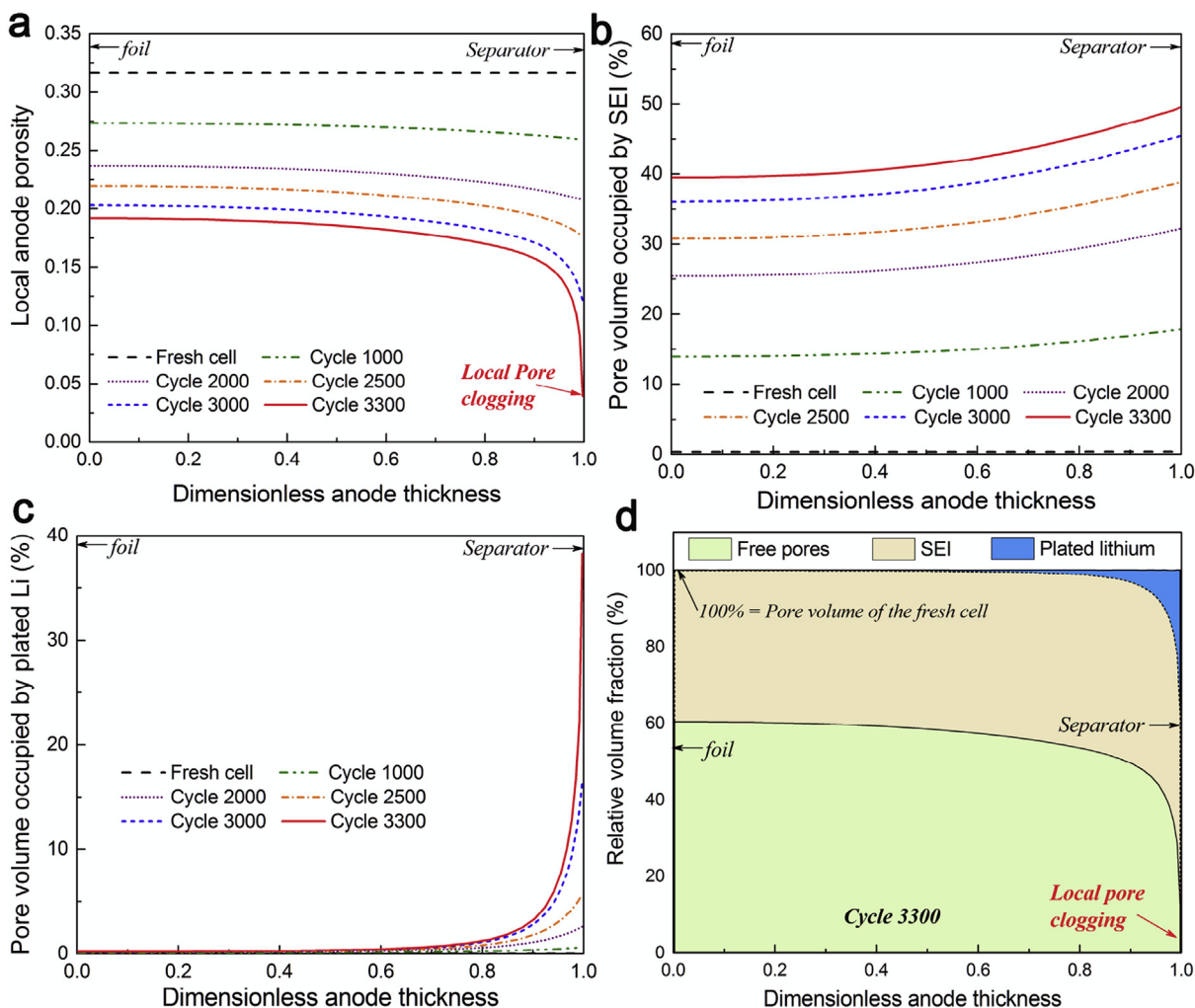


Fig. 5. Distributions of (a) local porosity, (b) fraction of pore volume occupied by SEI and (c) fraction of pore volume occupied by lithium metal along the thickness of anode in the cell after different number of cycles. (d) Relative volume fraction of free pores, SEI and lithium metal across the anode in the cell after 3300 cycles.

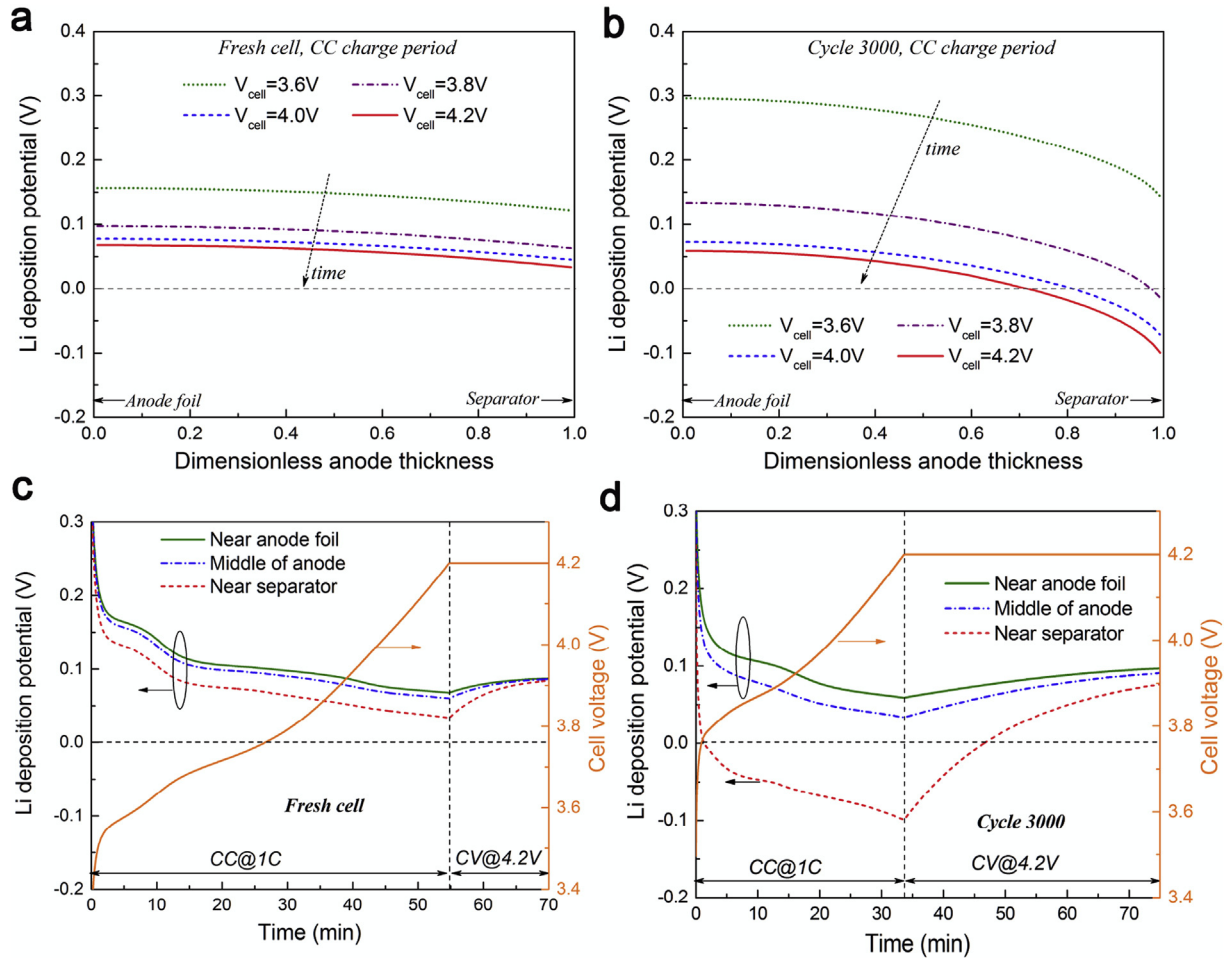


Fig. 6. (a&b) Distributions of lithium deposition potential (LDP) across the thickness of anode in the charge process of (a) the fresh cell and (b) the cell after 3000 cycles. (c–d) Evolution of the LDP at three different locations of the anode with time in the entire CCCV charge process of (c) the fresh cell and (d) the cell after 3000 cycles.

initial pore volume is occupied by the SEI layer after serious aging. In the meantime, a vast amount of lithium metal is plated in a region near the separator, leading to ultralow volume fraction of free pores. As such, conduction of ionic charges and diffusion of Li^+ ions are extremely difficult in the region near the separator, leading to high electrolyte resistance as shown in Fig. 4c.

Now with the understandings on the characteristics of porosity reduction over cycling, the behavior of voltage undershoot in Fig. 3d can be further elaborated. Several representative data points are selected from the 3C discharge curve of the cell after 3300 cycles, as marked and labeled in Fig. S1a of the supplementary material. Corresponding evolution of cell temperature is given in Fig. S1b. Furthermore, the distributions of electrolyte concentration, electrolyte potential, local current density of lithium deintercalation from graphite, and average lithium stoichiometry along the anode thickness in the discharge process are plotted in Figs. S1c–S1f respectively. At the beginning of discharge, almost all the current is generated in a fairly small portion of anode near the separator, as can be noted from Fig. S1e. This can be attributed to the clogging of pores near the separator which makes conduction and diffusion of Li^+ ions be extremely difficult in this region. As such, only a limited portion of the anode that is close to the separator is active for current generation at the beginning of discharge. To fulfill the demand for the 3C output current, a huge drop of electrolyte potential occurs near the anode/separator interface (Fig. S1d) to produce large local current density. A large number of

Li^+ ions are thus extracted from graphite near the separator, whereas the diffusivity of Li^+ ions is rather poor in this region due to the ultralow porosity. As a consequence, Li^+ ions accumulate in this region and form a local peak as can be seen from the concentration profiles shown in Fig. S1c. The locally high Li^+ concentration further aggravates the electrolyte potential drop near the separator because: a) the ionic conductivity is poorer at higher Li^+ concentrations; b) the diffusional ionic conductivity is high in concentrated solutions, inducing larger concentration overpotential. Therefore, the anode electrolyte resistance increases rapidly upon the start of discharge (Fig. 4c), leading to rapid drop of cell voltage (Fig. 3d). In the meantime, a great amount of heat is produced in this process due to the high current and low voltage, resulting in rapid rise of cell temperature as shown in Fig. S1b. The increase of temperature is able to enhance both the electrolyte conductivity and diffusivity, which offsets the negative impacts associated with the rising electrolyte concentration. As a result, cell voltage bounces back after reaching a local minimum, and distributions of concentration, potential and current density become more uniform across the anode.

4.3. Characteristics of lithium plating over cycling

It can be concluded from the above section that the rapid drop of the 2C capacity in Fig. 2a after extended cycling is attributed to the sharp reduction of local porosity near the separator which induces

significant increase of anode electrolyte resistance. The rapid drop of local porosity is ascribed to the large amount of lithium metal plated near the separator in the late stage of cycling. In this section, the characteristics of lithium plating are discussed in detail.

As indicated by Eq. (12), the rate of lithium deposition reaction depends highly on the lithium deposition potential (LDP), defined as $\phi_s - \phi_e - j_{tot} * R_{film} / a$. The solid-phase potential is close to zero in the anode, and the resistance of surface film is small at room temperature. The LDP is therefore strongly affected by the electrolyte potential. Fig. 6a and b presents the distributions of LDP in the anode during the 1C charge process of the fresh cell and of the cell after the 3000th cycle. Corresponding distributions of electrolyte potential in the anode are given in Fig. S2. As the ionic current moves from cathode to anode during charging, the electrolyte potential in the anode is highest near the separator and lowest near the foil. Accordingly, the LDP decreases from the anode foil to the anode/separator interface. In the charging process of the fresh cell, as shown in Fig. 6a, the LDP is fairly uniform and much higher than 0 V vs Li/Li⁺ across the anode, indicating that no lithium plating occurs in the fresh cell. In the charging process of the aged cell after 3000 cycles, however, there is dramatic rise of electrolyte potential in the anode, especially in the region near the separator. The LDP therefore drops greatly across the anode, and even becomes negative in a

region close to the separator at high cell voltages, as can be seen from Fig. 6b, which would result in lithium deposition. To better understand the behavior of lithium plating over the entire charging process, we plot in Fig. 6c and d the evolutions of LDP with time at three different locations of the anode in the CCCV charging process of the two cells in Fig. 6a and b. The variation of cell voltage is also plotted for reference. In both cases, the LDP at each selected position drops during CC charging and approaches its minimum at the time of reaching the cut-off voltage (4.2 V), and then bounces back. In summary of Fig. 6, we can learn that lithium plating is more prone to occur near the anode/separator interface due to the highest electrolyte potential (lowest LDP) there. Furthermore, in terms of temporal evolution over the charging process, lithium plating is most serious at the time of reaching the cut-off voltage. In the following, the time of reaching cut-off voltage, and the position of anode/separator interface are selected to study the spatial and temporal characteristics of lithium plating during cell aging.

Fig. 7a presents the distributions of LDP in the anode at the time of reaching cut-off voltage in the CCCV charging process of the cell after different cycle numbers. It can be noted that the drop of LDP across the anode becomes steeper as the cycling proceeds, leading to much lower LDP at the anode/separator interface in more aged cells. This can be attributed to the sharper rise of the electrolyte

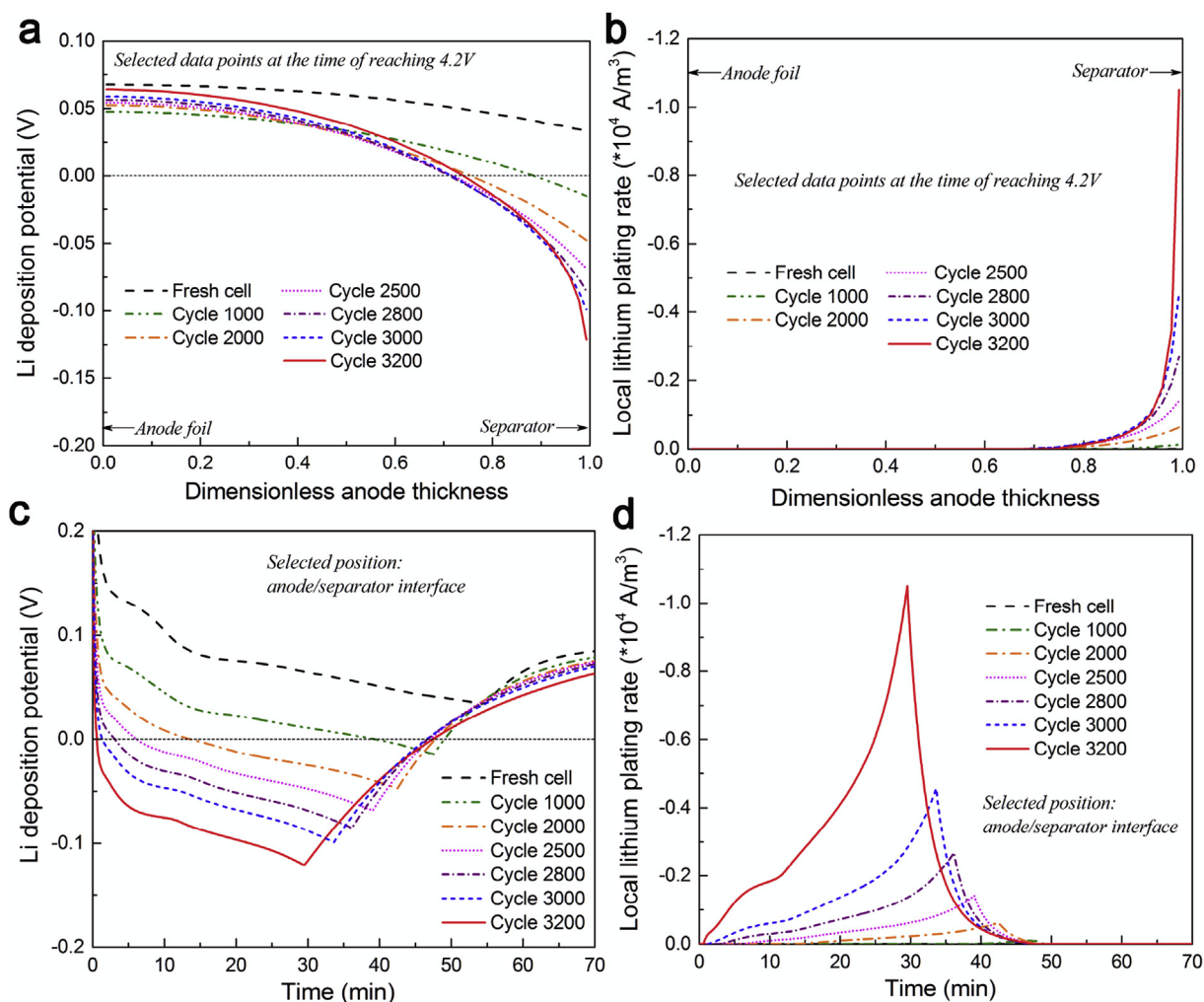


Fig. 7. (a&b) Distributions of (a) lithium deposition potential (LDP) and (b) lithium plating current density along the thickness of anode at the time of reaching the cut-off voltage in the CCCV charge process of the cell after different number of cycles. (c&d) Evolutions of LDP and lithium plating current density with time at the anode/separator interface in the CCCV charge process of the cell at different aging states.

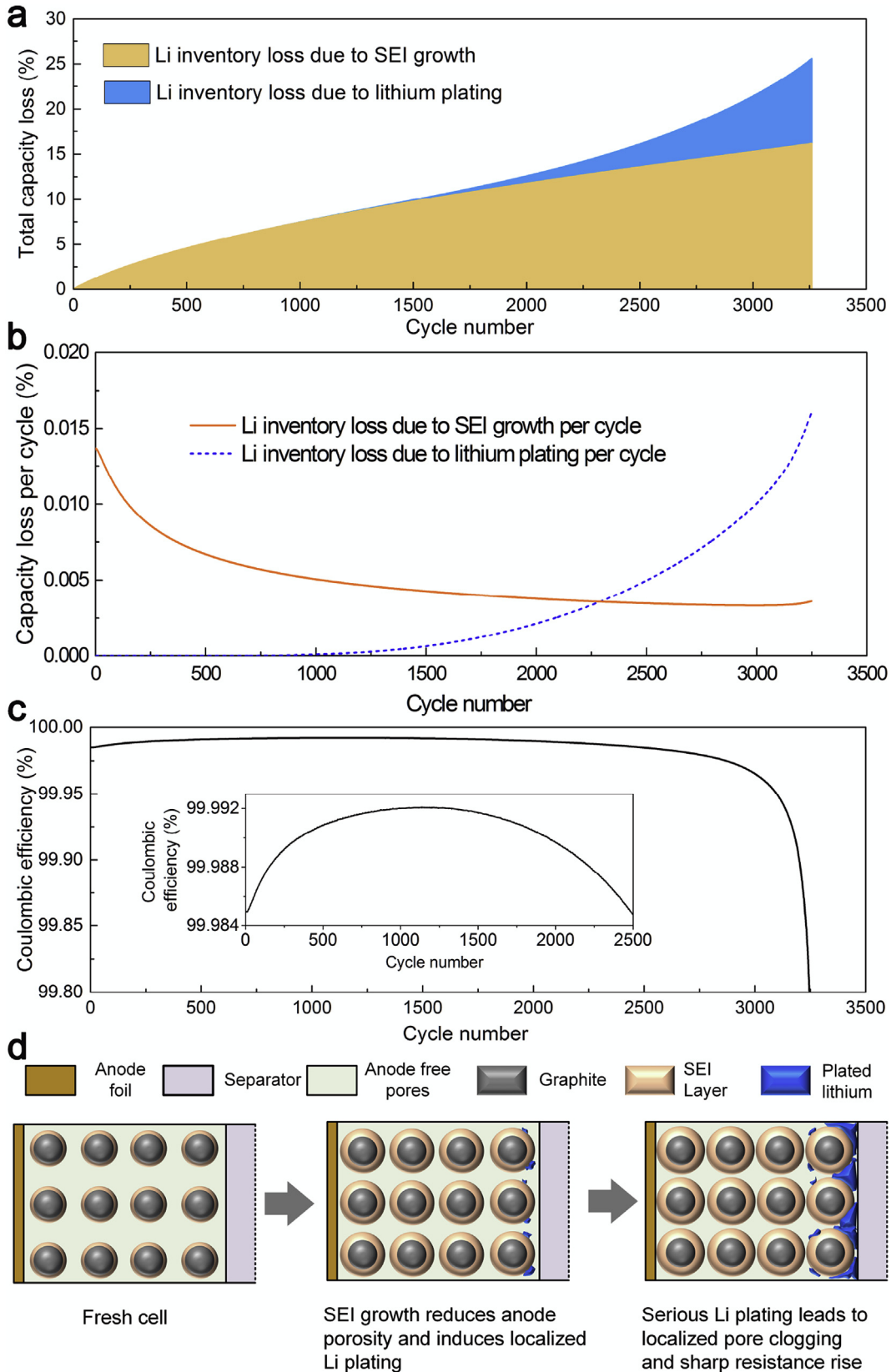


Fig. 8. (a–c) Variation of (a) overall capacity loss, (b) capacity loss in each cycle contributed by SEI growth and lithium plating, and (c) coulombic efficiency (CE) respectively in the cycling process. The inset in (c) is an enlarged view of the CE within the first 2500 cycles. (d) Schematic illustration of the aging behavior of a cell undergoing prolonged cycling with transition from linear to nonlinear aging.

potential across the anode over cycling as can be seen from Fig. 53. The increase in the gradient of electrolyte potential across anode over cycling can be further ascribed to the drop of anode porosity as shown in Fig. 5a, which reduces both electrolyte conductivity and diffusivity. As such, lithium plating starts to occur after a certain number of cycles and becomes serious afterwards, as can be noted from Fig. 7b, where the distributions of local reaction rate of lithium plating along the anode thickness are plotted. It can be learned from this figure that lithium plating, occurring in a narrow portion of anode near the separator, starts to be notable after ~2500 cycles and becomes extremely serious after ~3000 cycles. This rapid rise of lithium plating rate with cycle number in the late stage of cycling is ascribed to the interaction between lithium plating and porosity drop. As mentioned earlier, the drop of porosity due to surface film growth reduces electrolyte conductivity and thus aggravates the gradient of electrolyte potential in the anode, leading to lower LDP near the anode/separator interface. The rate of lithium plating, as described by Eq. (12), depends exponentially on the LDP, and therefore increases drastically with the drop of porosity. A large amount of lithium metal is thus generated, as shown in Fig. 5c, which further accelerates the drop of anode porosity. As such, the positive feedback between the drop of porosity and the increase of lithium plating rate result in sharp drop of porosity near the anode/separator (Fig. 5a), and exponential increase of lithium plating rate (Fig. 7b) in the final stage of cycling.

Fig. 7c and d further plot the temporal evolutions of LDP and lithium plating rate at the anode/separator interface over the CCCV charging process of the cell after different number of cycles. It can be noted that the length of time during which lithium plating occurs increases as the cycling proceeds. Based on the spatial (Fig. 7b) and temporal (Fig. 7d) variations of lithium plating rate, it can be concluded that both the area of anode suffering from lithium plating and length of time during which lithium plating occurs increase in the cycling process. We shall note that the integration of lithium plating current density (in A/m^3) over time and volume is the capacity (in Ah) lost due to lithium plating.

Fig. 8a present the variation of total capacity loss with the cycle number. Here the capacity loss refers to loss of lithium inventory, and is broken down to into those contributed by SEI formation and by lithium plating respectively. The capacity losses in each cycle due to the two mechanisms are plotted in Fig. 8b, and the variation of coulombic efficiency (CE) with cycle number is given in Fig. 8c. It can be seen from Fig. 8b that lithium plating is negligible in the early stage of cycling (e.g. <1500 cycles); thus almost all the capacity loss is attributed to SEI growth in this process, as shown in Fig. 8a. The decreasing rate of SEI growth leads to increasing CE in the early stage of cycling, as can be seen from the inset in Fig. 8c. As the cycling proceeds, lithium plating starts to occur. The rate of lithium plating increases exponentially with cycle number, due to the positive feedback between porosity drop and lithium plating rate increase as discussed above. When the increase of lithium plating rate outpaces the decrease of SEI growth rate, the overall aging rate starts to increase, leading to drop of CE as can be seen from the inset in Fig. 8c. In the late stage of cycling, lithium plating becomes the dominant mechanism for lithium inventory loss, as shown in Fig. 8b, and the steep rise of lithium plating rate results in sharp drop of CE as shown in Fig. 8c. It can be drawn that high precision measurement of CE is a possible method for online detection of lithium plating, as proposed by Jeff Dahn's group [63].

To sum up, the aging behavior of a cell undergoing prolonged cycling can be described by the sketch in Fig. 8d. In the early stage of cycling, cell aging is dominated by the SEI growth, which leads to linear drop of cell capacity with cycle number and slow rise of cell resistance. The growth of SEI layer reduces the anode porosity, leading to larger gradient of electrolyte potential in the anode and

thus lower LDP at the anode/separator interface in charging process. After a number of cycles, the LDP in cell charging becomes negative vs Li/Li^+ in a portion of anode near the separator, triggering lithium plating. Deposition of lithium metal contributes to the drop of local porosity, while the drop of porosity further enhances lithium plating rate by aggravating the gradient of electrolyte potential in the anode. The positive feedback between the increase of lithium plating rate and the decrease of local porosity results in exponential rise of lithium plating rate and sharp drop of local anode porosity simultaneously, leading to nonlinear lithium inventory loss and resistance rise.

5. Conclusion

We have presented a physics-based Li-ion battery model able to predict the aging characteristics of Li-ion cells associated with lithium plating. Both SEI growth and lithium plating are included in the model, and the ensuing reduction of anode porosity during aging is also incorporated. The model is applied to study the aging behavior of a plug-in EV battery undergoing prolonged cycling at room temperature with moderate charge/discharge current. Cell aging is found to be linear with cycle number in the early stage of cycling, during which cell capacity drops linearly while cell resistance increases only slightly. SEI growth is found to be the dominant aging mechanism in this linear aging stage. As the cycling proceeds, the anode porosity drops due to continuous SEI growth, leading to larger gradient of electrolyte potential in the anode, and therefore to lower lithium deposition potential (LDP) in the charge process. After a certain number of cycles, the LDP in cell charging would drop below 0 V vs Li/Li^+ , leading to onset of lithium plating. The lithium deposition reaction is found to occur only in a narrow region close to the anode/separator interface due to the highest electrolyte potential (lowest LDP) there during charging. The appearance of lithium metal further accelerates the reduction of local anode porosity, leading to larger gradient of electrolyte potential in the anode, and accordingly to lower LDP and higher lithium plating rate. This positive feedback between the increase of lithium plating rate and the decrease of anode porosity results in exponential rise of lithium plating rate as well as sharp drop of local porosity near the anode/separator interface simultaneously. As a consequence, cell aging transits from linear to nonlinear. The dramatic increase of lithium plating rate leads to rapid loss of lithium inventory. In the meantime, the clogging of pores near the separator induces substantial rise of anode electrolyte resistance, which also leads to an interesting behavior of voltage undershoot in the discharge curves of the seriously aged cells at high rate.

Acknowledgements

Partial financial support by Pennsylvania Department of Environmental Protection, Diefenderfer Chair Endowment, DOE CAE-BAT Program under award number DE-EE0006425 and BMW Group is gratefully acknowledged. We are also grateful to EC Power for offering numerical algorithms and materials database through its AutoLion™ software.

Appendix A. Supplementary data

Supplementary data related to this article can be found at <http://dx.doi.org/10.1016/j.jpowsour.2017.05.110>.

References

- [1] V. Etacheri, R. Marom, R. Elazari, G. Salitra, D. Aurbach, *Energy Environ. Sci.* 4 (2011) 3243–3262.

- [2] M.R. Palacín, A. de Guibert, Science 351 (2016) 1253292.
- [3] J. Vetter, P. Novák, M.R. Wagner, C. Veit, K.C. Möller, J.O. Besenhard, M. Winter, M. Wohlfahrt-Mehrens, C. Vogler, A. Hammouche, J. Power Sources 147 (2005) 269–281.
- [4] A. Barré, B. Deguilhem, S. Grolleau, M. Gérard, F. Suard, D. Riu, J. Power Sources 241 (2013) 680–689.
- [5] T. Yoshida, M. Takahashi, S. Morikawa, C. Ihara, H. Katsukawa, T. Shiratsuchi, J.-i. Yamaki, J. Electrochem. Soc. 153 (2006) A576–A582.
- [6] D. Lin, Y. Liu, Y. Cui, Nat. Nano 12 (2017) 194–206.
- [7] L. Mai, X. Tian, X. Xu, L. Chang, L. Xu, Chem. Rev. 114 (2014) 11828–11862.
- [8] X. Liu, J.Q. Huang, Q. Zhang, L. Mai, Adv. Mater. (2017) 1601759.
- [9] A. Farmann, W. Waag, A. Marongiu, D.U. Sauer, J. Power Sources 281 (2015) 114–130.
- [10] F. Sun, R. Xiong, H. He, J. Power Sources 259 (2014) 166–176.
- [11] R. Xiong, F. Sun, Z. Chen, H. He, Appl. Energy 113 (2014) 463–476.
- [12] W.H. Woodford, Y.M. Chiang, W.C. Carter, J. Electrochem. Soc. 157 (2010) A1052–A1059.
- [13] J. Zhang, B. Lu, Y. Song, X. Ji, J. Power Sources 209 (2012) 220–227.
- [14] X.G. Yang, C. Bauer, C.Y. Wang, J. Power Sources 327 (2016) 414–422.
- [15] C. Zhan, J. Lu, A. Jeremy Kropf, T. Wu, A.N. Jansen, Y.-K. Sun, X. Qiu, K. Amine, Nat. Commun. 4 (2013) 2437.
- [16] J. Lu, C. Zhan, T. Wu, J. Wen, Y. Lei, A.J. Kropf, H. Wu, D.J. Miller, J.W. Elam, Y.K. Sun, X. Qiu, K. Amine, Nat. Commun. 5 (2014) 5693.
- [17] Y. Zhang, C.Y. Wang, J. Electrochem. Soc. 156 (2009) A527–A535.
- [18] R.V. Bugga, M.C. Smart, ECS Trans. 25 (2010) 241–252.
- [19] Z. Li, J. Huang, B. Yann Liaw, V. Metzler, J. Zhang, J. Power Sources 254 (2014) 168–182.
- [20] M. Petzl, M. Kasper, M.A. Danzer, J. Power Sources 275 (2015) 799–807.
- [21] T. Waldmann, M. Wilka, M. Kasper, M. Fleischhammer, M. Wohlfahrt-Mehrens, J. Power Sources 262 (2014) 129–135.
- [22] M. Dubarry, B.Y. Liaw, J. Power Sources 194 (2009) 541–549.
- [23] P. Liu, J. Wang, J. Hicks-Garner, E. Sherman, S. Soukiazian, M. Verbrugge, H. Tatarija, J. Musser, P. Finamore, J. Electrochem. Soc. 157 (2010) A499–A507.
- [24] M. Dubarry, C. Truchot, B.Y. Liaw, J. Power Sources 258 (2014) 408–419.
- [25] J. Wang, J. Purewal, P. Liu, J. Hicks-Garner, S. Soukiazian, E. Sherman, A. Sorenson, L. Vu, H. Tatarija, M.W. Verbrugge, J. Power Sources 269 (2014) 937–948.
- [26] M. Ecker, N. Nieto, S. Kabitz, J. Schmalstieg, H. Blanke, A. Warnecke, D.U. Sauer, J. Power Sources 248 (2014) 839–851.
- [27] S.F. Schuster, T. Bach, E. Fleder, J. Müller, M. Brand, G. Sextl, A. Jossen, J. Energy Storage 1 (2015) 44–53.
- [28] J.C. Burns, A. Kassam, N.N. Sinha, L.E. Downie, L. Solnickova, B.M. Way, J.R. Dahn, J. Electrochem. Soc. 160 (2013) A1451–A1456.
- [29] Y. Leng, S. Ge, D. Marple, X.G. Yang, C. Bauer, P. Lamp, C.Y. Wang, J. Electrochem. Soc. 164 (2017) A1037–A1049.
- [30] M. Klett, R. Eriksson, J. Groot, P. Svens, K. Ciosek Högstöm, R.W. Lindström, H. Berg, T. Gustafson, G. Lindbergh, K. Edström, J. Power Sources 257 (2014) 126–137.
- [31] M. Klett, P. Svens, C. Tengstedt, A. Seyeux, J. Świątowska, G. Lindbergh, R. Wreland Lindström, J. Phys. Chem. C 119 (2015) 90–100.
- [32] E. Sarasketa-Zabala, F. Aguesse, I. Villarreal, L.M. Rodriguez-Martinez, C.M. López, P. Kubiak, J. Phys. Chem. C 119 (2015) 896–906.
- [33] M. Lewerenz, J. Münnich, J. Schmalstieg, S. Käbitz, M. Knips, D.U. Sauer, J. Power Sources 345 (2017) 254–263.
- [34] M. Broussely, P. Biensan, F. Bonhomme, P. Blanchard, S. Herreyre, K. Nechev, R.J. Staniewicz, J. Power Sources 146 (2005) 90–96.
- [35] L. Yang, X. Cheng, Y. Gao, Y. Ma, P. Zuo, C. Du, Y. Cui, T. Guan, S. Lou, F. Wang, W. Fei, G. Yin, RSC Adv. 4 (2014) 26335–26341.
- [36] M. Dubarry, C. Truchot, B.Y. Liaw, K. Gering, S. Sazhin, D. Jamison, C. Michelbacher, J. Power Sources 196 (2011) 10336–10343.
- [37] M. Zier, F. Scheiba, S. Oswald, J. Thomas, D. Goers, T. Scherer, M. Klose, H. Ehrenberg, J. Eckert, J. Power Sources 266 (2014) 198–207.
- [38] J.T. Lee, N. Nitta, J. Benson, A. Magasinski, T.F. Fuller, G. Yushin, Carbon 52 (2013) 388–397.
- [39] S. Frisco, A. Kumar, J.F. Whitacre, S. Litster, J. Electrochem. Soc. 163 (2016) A2636–A2640.
- [40] G. Sikha, B.N. Popov, R.E. White, J. Electrochem. Soc. 151 (2004) A1104–A1114.
- [41] G. Ning, B.N. Popov, J. Electrochem. Soc. 151 (2004) A1584–A1591.
- [42] G. Ning, R.E. White, B.N. Popov, Electrochim. Acta 51 (2006) 2012–2022.
- [43] S. Santhanagopalan, Q. Guo, P. Ramadass, R.E. White, J. Power Sources 156 (2006) 620–628.
- [44] M. Safari, M. Morcrette, A. Teyssot, C. Delacourt, J. Electrochem. Soc. 156 (2009) A145–A153.
- [45] M.B. Pinson, M.Z. Bazant, J. Electrochem. Soc. 160 (2013) A243–A250.
- [46] M.T. Lawder, P.W.C. Northrop, V.R. Subramanian, J. Electrochem. Soc. 161 (2014) A2099–A2108.
- [47] P. Gambhire, K.S. Hariharan, A. Khandelwal, S.M. Kolake, T. Yeo, S. Doo, J. Power Sources 270 (2014) 281–291.
- [48] P. Arora, M. Doyle, R.E. White, J. Electrochem. Soc. 146 (1999) 3543–3553.
- [49] M. Tang, P. Albertus, J. Newman, J. Electrochem. Soc. 156 (2009) A390–A399.
- [50] R.D. Perkins, A.V. Randall, X. Zhang, G.L. Plett, J. Power Sources 209 (2012) 318–325.
- [51] H. Ge, T. Aoki, N. Ikeda, S. Suga, T. Isobe, Z. Li, Y. Tabuchi, J. Zhang, J. Electrochem. Soc. 164 (2017) A1050–A1060.
- [52] N. Legrand, B. Knosp, P. Desprez, F. Lapique, S. Raël, J. Power Sources 245 (2014) 208–216.
- [53] M. Doyle, T.F. Fuller, J. Newman, J. Electrochem. Soc. 140 (1993) 1526–1533.
- [54] W.B. Gu, C.Y. Wang, J. Electrochem. Soc. 147 (2000) 2910–2922.
- [55] V. Srinivasan, C.Y. Wang, J. Electrochem. Soc. 150 (2003) A98–A106.
- [56] W. Fang, O.J. Kwon, C.Y. Wang, Int. J. Energy Res. 34 (2010) 107–115.
- [57] X.G. Yang, G. Zhang, C.Y. Wang, J. Power Sources 328 (2016) 203–211.
- [58] X.G. Yang, T. Liu, C.Y. Wang, J. Power Sources 342 (2017) 598–604.
- [59] Y. Ji, Y. Zhang, C.Y. Wang, J. Electrochem. Soc. 160 (2013) A636–A649.
- [60] C.Y. Wang, T. Xu, S. Ge, G. Zhang, X.G. Yang, Y. Ji, J. Electrochem. Soc. 163 (2016) A1944–A1950.
- [61] J. Kalupson, G. Luo, C.E. Shaffer, SAE Tech. Pap. (2013), 01–1522.
- [62] AutoLion™, www.ecpowergroup.com/autolion/.
- [63] J.C. Burns, D.A. Stevens, J.R. Dahn, J. Electrochem. Soc. 162 (2015) A959–A964.

Nomenclature

- a : specific surface area, m^{-2}
 c : concentration, mol m^{-3}
 c_p : specific heat, $\text{J kg}^{-1} \text{K}^{-1}$
 D : diffusion coefficient, $\text{m}^2 \text{s}^{-1}$
 F : Faraday constant, 96487 C mol^{-1}
 h : convective heat transfer coefficient, $\text{W m}^{-2} \text{K}^{-1}$
 i_0 : exchange current density, A m^{-2}
 j : volumetric current density, A m^{-3}
 k : kinetic rate constant, m s^{-1}
 M : molecular weight, kg mol^{-1}
 Q : heat source, W
 r : coordinate in the radial direction, m
 R : resistance, Ω
 t : time, s
 t_+ : transference number
 T : temperature, K
 U : open-circuit potential, V

Greek

- α : charge transfer coefficient
 ϵ : porosity
 σ : electronic conductivity, S m^{-1}
 κ : electrolyte conductivity, S m^{-1}
 κ_D : diffusional conductivity, A m^{-1}
 ϕ : electric potential, V
 ρ : density, kg m^{-3}
 η : overpotential, V
 δ : thickness, m

Subscripts

- e : electrolyte phase
 EC : ethylene carbonate
 int : intercalation
 lpl : lithium plating
 s : solid phase, or surface
 SEI : solid-electrolyte interphase
 tot : total